



Ligand exchange of SnO₂ effectively improving the efficiency of flexible perovskite solar cells

Jia Dong^{a,b}, Jinbiao Jia^a, Xu Feng^c, Beibei Shi^a, Yangqing Wu^a, Yongzheng Zhang^a, Jihuai Wu^b, Bingqiang Cao^{a,*}

^a School of Physics and Physical Engineering, Shandong Provincial Key Laboratory of Laser Polarization and Information Technology, Qufu Normal University, Qufu 273165, China

^b Engineering Research Center of Environment-Friendly Functional Materials, Ministry of Education, Fujian Key Laboratory of Photoelectric Functional Materials, Huaqiao University, Xiamen 361021, China

^c School of Chemistry and Chemical Engineering, Qufu Normal University, Qufu 273165, China



ARTICLE INFO

Article history:

Received 25 March 2021

Received in revised form 27 May 2021

Accepted 12 June 2021

Available online 15 June 2021

Keywords:

SnO₂

Electron transport layer

Ligand exchange

Flexible perovskite solar cell

ABSTRACT

Owing to the advantages of portability and flexibility, flexible perovskite solar cells have broad application prospects in the fields of portable wearable electronics and photovoltaic buildings. However, high temperature annealing process is often needed to improve the crystallinity and electron transport properties for electron transport layer, which restricts the development of flexible perovskite solar cells. In this work, well crystalline and monodisperse SnO₂ nanocrystals are synthesized by facile solvothermal method with the assistance of oleic acid molecules. However, the presence of oleic acid molecules blocks the transportation of photogenerated electrons on account of the insulation of oleic acid molecules. To address the problem, the oleic acid ligands are ulteriorly peeled off by ligand exchange technique. Surprisingly, the resulted SnO₂ electron transport layer exhibits superior electron extraction and transport capacity. The final power conversion efficiency comes to 17.96% from 13.71%.

© 2021 Elsevier B.V. All rights reserved.

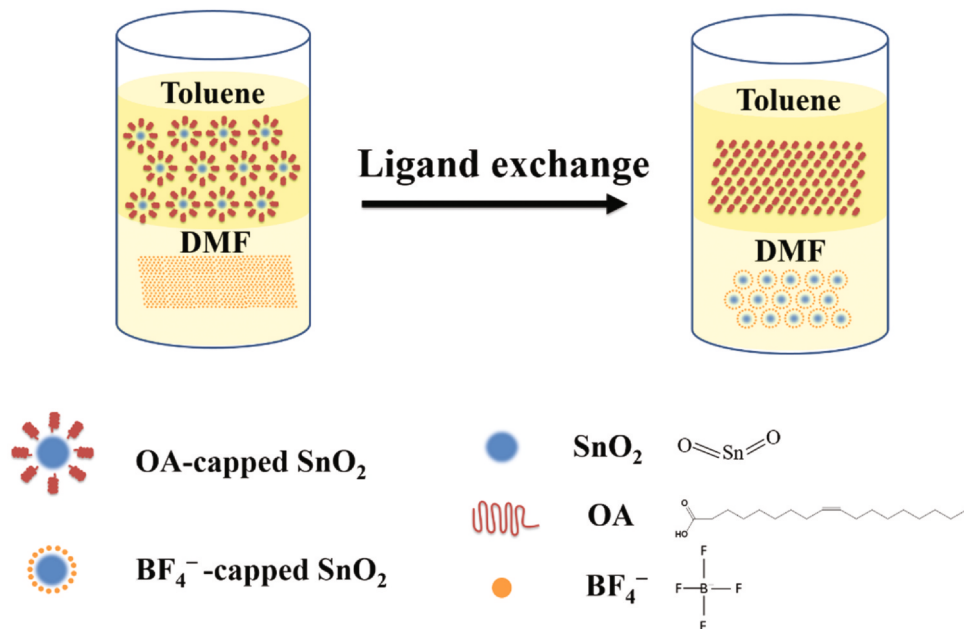
1. Introduction

In the past decade, organic-inorganic halide perovskite solar cells (PSCs) have been considered as one of the most promising photovoltaic devices due to their brilliant photoelectric properties such as high extinction coefficient, long diffusion length and high carrier mobility [1–5]. Moreover, PSCs can be combined with commercial silicon solar cells to form tandem architecture, which further improves the power conversion efficiency (PCE). Lately, the flexible structured PSCs (*f*-PSCs) attract increasing interest due to the rapid development of intelligent electronics industry [6,7]. *f*-PSCs are light in weight and have good bending resistance, representing unique applications in wearable electronic equipment and bendable displays. Although the *f*-PSC exhibits broad application prospects, the development of *f*-PSC is relatively slow compared to that of the rigid PSC device. So far, the latest certification report shows that the PCE of a single PSC on glass substrate has been up to 25.5%, which is almost comparable to that of the commercial silicon cell [8].

However, the highest PCE of *f*-PSC devices is only 21.7% [9]. The main challenge for *f*-PSCs is that the charge extraction layer under perovskite light-absorption layer is difficult to fabricate as the most commonly used flexible conductive substrates, polyethylene naphthalate (PEN) and poly(ethylene terephthalate) (PET), cannot withstand high temperature procedure. Under high temperature conditions, the two flexible substrates are prone to irreversible deformation and bending. As a consequence, for *f*-PSC devices, all the functional layers must be fabricated at limited low temperature (usually below 150 °C) [10]. At the moment, the PSC devices have two classic structures, n-i-p configuration (normal structure) and p-i-n configuration (inverted structure). While high-efficiency PSC device usually opts for normal structure and prefers to use TiO₂ as the electron transport material [11–14]. However, TiO₂ always requires high-temperature sintering procedure, otherwise severe hysteresis will occur in the device. Later, SnO₂ appears as an effective electron transport material for PSC devices. The wide bandgap semiconductor, SnO₂, has high electron mobility, and its energy band matches well with perovskite light-absorption materials. In parallel, SnO₂ electron transport layer (ETL) can be fabricated through varieties of low temperature preparation process, such as solution spin-coating procedure [15,16], thermal-evaporation process [17],

* Corresponding author.

E-mail address: caobq@qfnu.edu.cn (B. Cao).



Scheme 1. Illustration of the ligand exchange procedure.

electron beam evaporation deposition [18], atomic-layer deposition [19,20], etc. According to the previous report, compared to the SnO_2 ETL annealed at 500 °C, low-temperature annealed SnO_2 ETL (185 °C) has more efficient electron transmission capability [21]. Consequently, these advantages allow researchers to explore the potential application of low-temperature processed SnO_2 in *f*-PSC with n-i-p structure. Combining spin-coating process with hydrothermal treatment method, Xu et al. fabricated ligand-free and highly crystalline SnO_2 ETL at low temperature. The obtained n-i-p structured *f*-PSC received a certificated PCE of 17.3% [22]. Using sol-gel and spin-coating process, Wang et al. prepared SnO_2 ETL with satisfying morphology and crystallinity. The resulted n-i-p structured *f*-PSC yielded a PCE of 17.5% [23].

In this study, well crystalline and monodisperse SnO_2 nanocrystals were obtained by a simple solvent thermal method under the assistance of oleic acid (OA) molecules. Although the introduction of OA ligands regulated the growth of SnO_2 nanocrystals and assisted SnO_2 nanocrystals re-dispersed in toluene to form spin-coating solution, the long chain of OA ligands separated SnO_2 nanocrystals, and created insulating barriers around SnO_2 nanocrystals, which blocked the collection and transmission of electrons. As a result, the *f*-PSC assembled with the as-prepared SnO_2 ETL only received a PCE of 13.71%. Thereafter, to address this problem, we used ligand-exchange process to replace the long chain OA ligands with BF_4^- . Surprisingly, the BF_4^- short chain ligands modified SnO_2 can be well re-dispersed in N,N-Dimethylformamide (DMF) to form spin-coating solution. The spin-coated SnO_2 ETL exhibited enhanced interparticle interaction, and acquired improved conductivity, displaying excellent electron extraction and transport property. Finally, we obtained a well-behaved SnO_2 based *f*-PSC with 17.96% efficiency.

2. Experimental section

2.1. Materials

The flexible conductive substrate (PET) ($14 \Omega \text{ sq}^{-1}$) was purchased from Pilkington. Tin(IV) chloride pentahydrate, OA, cyclohexane, octadecenylamine, absolute ethanol, toluene and DMF were purchased from Sinopharm Chemical Reagent Co., Ltd China.

Nitrosonium tetrafluoroborate (NOBF_4) was purchased from Sigma-Aldrich.

2.2. Preparation of the spin-coating solution of SnO_2 nanocrystals

Firstly, the OA-capped SnO_2 nanocrystals were synthesized by a low cost solvothermal procedure. To gain high-quality SnO_2 colloidal nanocrystals, the long hydrocarbon molecule of OA, which plays a crucial role in the self-assembly of ordered SnO_2 nanocrystals, is introduced into the reaction precursor. The specific preparation process is as follows. 1.0 g Tin(IV) chloride pentahydrate was dissolved in the mixture of 7 mL OA, 20 mL cyclohexane and 5 mL octadecenylamine. Then the mixed solution was transferred into a 50 mL autoclave and reacted at 180 °C for 24 h. After cooling to room temperature, the products were precipitated and washed by absolute ethanol. Subsequently, the products were separated by centrifugation at 12,000 rpm for 10 min. The obtained products were re-dispersed in toluene to form the spin-coating solution of OA-capped SnO_2 nanocrystals with a concentration of 20 mg mL⁻¹.

The OA ligands in the spin-coating solution of OA-capped SnO_2 nanocrystals were removed and exchanged by BF_4^- anions according to the report [24]. In the typical procedure, 10 mL NOBF_4 solution of DMF (2 mg mL⁻¹) were mixed with 10 mL OA-capped SnO_2 nanocrystals solution of toluene (40 mg mL⁻¹) and stirred vigorously for 5 min. As a result, the OA-free and BF_4^- -capped SnO_2 nanocrystals were transferred into DMF phase. The BF_4^- -capped SnO_2 nanocrystals were precipitated and purified by toluene. The resulted BF_4^- -capped SnO_2 nanocrystals were re-dispersed in DMF to form the spin-coating solution of BF_4^- -capped SnO_2 nanocrystals with a concentration of 20 mg mL⁻¹. **Scheme 1** illustrates the ligand exchange process.

2.3. Solar cell fabrication

The etched PET substrates were consecutively ultrasonic cleaned with detergent aqueous solution, isopropanol and ethanol. Thereafter the substrates were dried with nitrogen gas flow and treated with plasma for 5 min. The OA-capped SnO_2 and BF_4^- -capped SnO_2 films were respectively deposited by spin-coating their

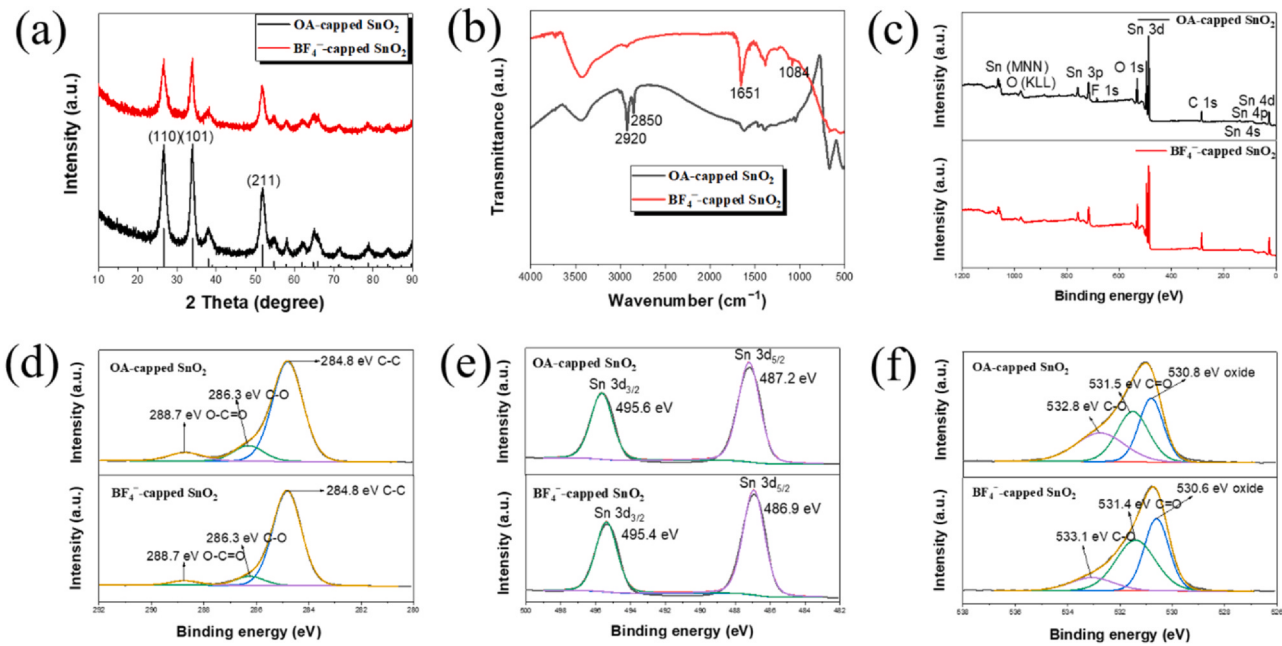


Fig. 1. (a) XRD patterns and (b) FTIR spectra of OA-capped and BF_4^- -capped SnO_2 nanocrystals, (c–f) XPS spectra of (c) survey scan, (d) C 1s scan, (e) Sn 3d scan, and (f) O 1s scan.

corresponding solution and then dried under 100 °C. The $\text{Cs}_{0.05}(\text{MA}_{0.17}\text{FA}_{0.83})_{0.95}\text{Pb}(\text{I}_{0.83}\text{Br}_{0.17})_3$ perovskite light-absorption layers, spiro-OMeTAD hole transport layers and Au electrodes were prepared according to our previous work [25,26].

2.4. Characterizations and measurements

The crystal structure of SnO_2 and perovskite on different SnO_2 ETLs were determined by X-Ray Diffraction (XRD). The interactions between SnO_2 nanocrystals and ligands were conducted with Fourier transform infrared spectroscopy (FTIR) and X-ray photo-electron spectroscopy (XPS). The morphology and structural features of the two SnO_2 nanocrystals were studied by using high resolution transmission electron microscopy (HRTEM). The wettability of perovskite precursor solution on SnO_2 ETL was conducted on a contact angle analyzer. The surface morphology of perovskite on different SnO_2 ETLs was observed by field emission scanning electron microscopy (FESEM). Current density-voltage (J-V) curves, external quantum efficiency (EQE), transient photocurrent/photovoltage decay (TPC/TPV) measurements were carried out by using the same method in our previous work [25,26]. Steady-state photoluminescence (SSPL) and time-resolved photoluminescence (TRPL) measurements were conducted by steady and transient fluorescence spectrometer (FLS1000, Edinburgh Instruments). Electrochemical impedance spectroscopy (EIS) was conducted under dark conditions at frequencies ranging from 1 MHz to 100 mHz with 15 mV AC amplitude using the P3000A electrochemical workstation produced by Ametek. Capacitance-frequency (C-F) curves was measured under AM 1.5G sunlight illumination with Keithley 4200A-SCS. In this work, the effective area of the f-PSC was about 0.1 cm².

3. Results and discussion

3.1. Composition analysis

XRD patterns were implemented to investigate the compositions and crystal structure of the products. The results are shown in Fig. 1(a). The XRD characterization in Fig. 1(a) confirms the good crystallinity of the two SnO_2 nanocrystals. Meanwhile, it can be observed that the two samples exhibit similar XRD patterns, which

indicates the same composition and crystal phase. By comparison with the standard card library, the two patterns match well with the tetragonal rutile-structured SnO_2 (PDF#41-1445). The three major diffraction peaks locate at 26.6°, 33.9° and 51.8°, which respectively correspond to the crystal planes of (110), (101) and (211). The XRD results indicate that the ligand-exchange treatment in this experiment will not affect the integrity of the SnO_2 crystal structure.

To confirm ligand-exchange, the native OA-capped SnO_2 and the exchanged BF_4^- -capped SnO_2 were characterized by FTIR spectroscopy and XPS survey. The FTIR spectra are given in Fig. 1(b). Fig. 1(b) shows that the intensity of the C–H stretching vibration peaks ($2800\text{--}3000\text{ cm}^{-1}$) is noticeably reduced after NOBF_4 modification, indicating that the OA molecules are effectively removed [27]. After ligand exchange, a strong peak at 1651 cm^{-1} appears, which is assigned to the C=O stretching vibration of DMF molecule [27]. Furthermore, the characteristic peak of BF_4^- anions at 1084 cm^{-1} can also be observed in the FTIR spectrum of BF_4^- -capped SnO_2 [28]. The results in FTIR spectra reveal that the ligand exchange reaction in this experiment was carried out effectively.

The ligand exchange of OA by BF_4^- on the surface of SnO_2 nanocrystals was also confirmed by XPS spectra. Fig. 1(d) shows the high resolution XPS spectra of C 1s. The spectrum of OA-capped SnO_2 nanocrystals shows the peaks at 284.8, 286.3 and 288.7 eV respectively correspond to C–C, C–O–C and O=C–O groups [29,30]. As for the sample of BF_4^- -capped SnO_2 nanocrystals, the C 1s XPS spectra show the same peak positions. While the peak intensity and peak area associated with O=C–O groups gest significantly decreased. In this experiment, O=C–O groups mainly come from OA molecules. Hence, the results in C 1s XPS spectra indicate that the OA ligands on the surface of SnO_2 are significantly reduced after ligands exchange procedure. Fig. 1(e) shows the high-resolution XPS spectra of Sn 3d. As for OA-capped SnO_2 nanocrystals, the Sn 3d high-resolution spectrum exhibits two symmetrical peaks located at 487.2 and 495.6 eV, which is related to the $\text{Sn 3d}_{5/2}$ and $\text{Sn 3d}_{3/2}$ characteristic peaks of SnO_2 [31–33]. While for BF_4^- -capped SnO_2 nanocrystals, the binding energy of $\text{Sn 3d}_{5/2}$ and $\text{Sn 3d}_{3/2}$ spin-orbit peaks are 486.9 and 495.4 eV, respectively. The small shift in the Sn 3d core level may be attributed to the variation of the surroundings around SnO_2 molecules, indicating that the ligands successfully exchange. Fig. 1(f) shows the high resolution XPS spectra of O 1s. The binding energies

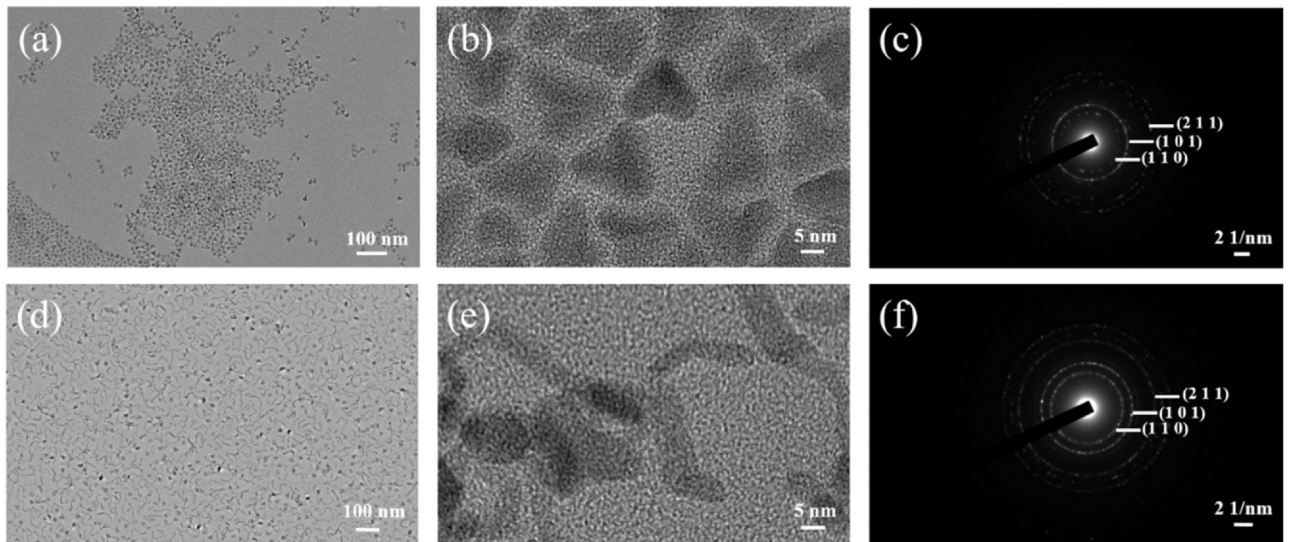


Fig. 2. (a) TEM and (b) HRTEM images of OA-capped SnO_2 nanocrystals, (c) SAED pattern of OA-capped SnO_2 nanocrystals, (d) TEM and (e) HRTEM images of BF_4^- -capped SnO_2 nanocrystals, (f) SAED pattern of BF_4^- -capped SnO_2 nanocrystals.

at 530.8 and 530.6 eV can be respectively attributed to the O^{2-} species in OA-capped SnO_2 nanocrystals and BF_4^- -capped SnO_2 nanocrystals [34,35]. In addition, the binding energies of $\text{C}=\text{O}$ and $\text{C}-\text{O}$ are also different, which is mainly ascribed to the different surrounding environment that $\text{C}=\text{O}$ and $\text{C}-\text{O}$ species lie in.

3.2. Morphology observation

The TEM images of SnO_2 nanocrystals before and after ligand exchange are shown in Fig. 2. Interestingly, the sample of OA-capped SnO_2 nanocrystals shown in Fig. 2(a, b) gives uniform heart-shaped

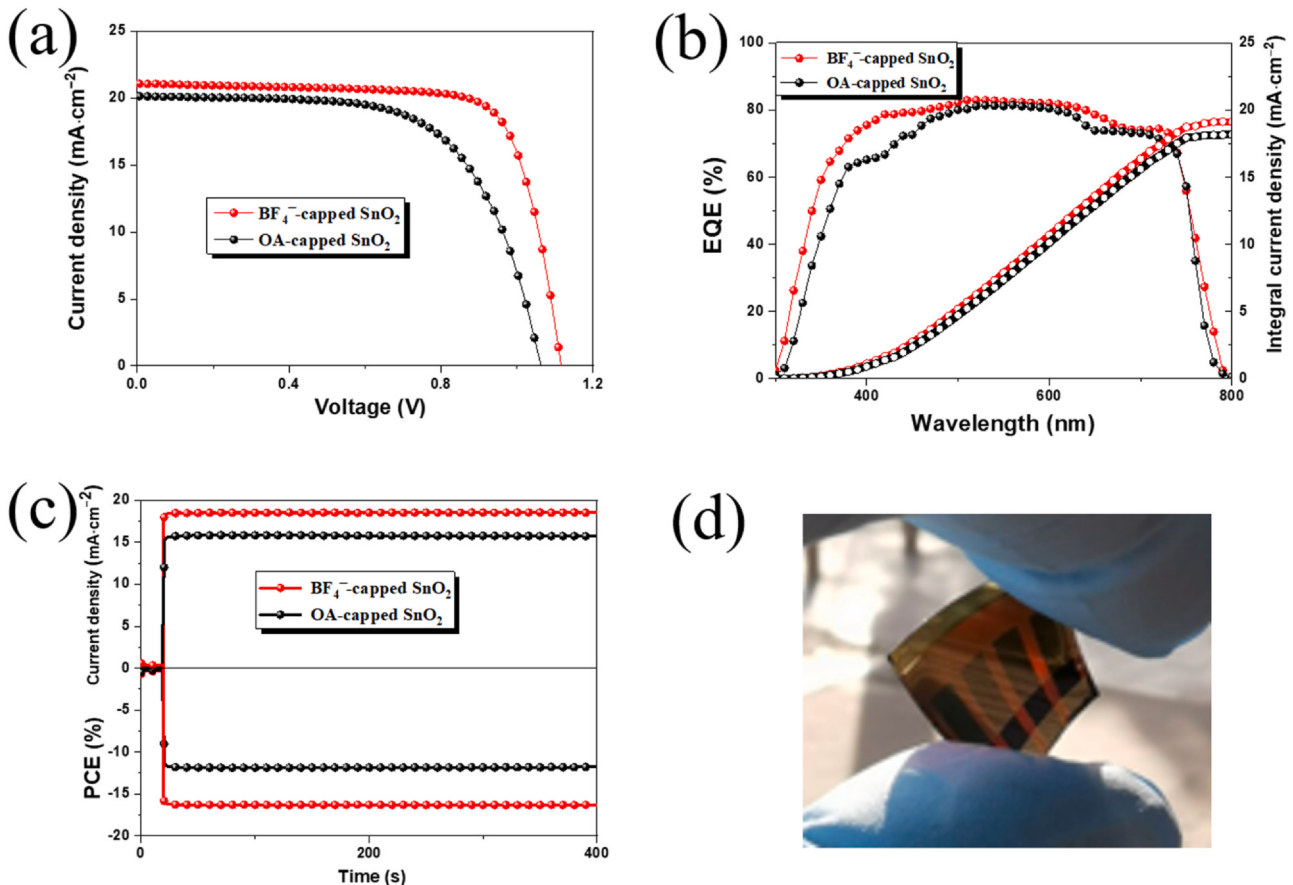


Fig. 3. (a) J-V curves of the best-behaved f-PSCs assembled with OA-capped SnO_2 and BF_4^- -capped SnO_2 , (b) EQE spectra of the above mentioned f-PSCs, (c) steady-state output of the f-PSCs fabricated with OA-capped SnO_2 and BF_4^- -capped SnO_2 tracking for 400 s, (d) photograph of the f-PSC with BF_4^- -capped SnO_2 ETL.

Table 1

Photovoltaic parameters of the *f*-PSCs with different SnO₂ ETLs.

ETLs	Scanning direction	V _{OC} (V)	J _{SC} (mA cm ⁻²)	FF	PCE (%)
OA-capped SnO ₂	reverse scan	1.063	20.12	0.641	13.71
BF ₄ ⁻ -capped SnO ₂	reverse scan	1.116	21.43	0.751	17.96

morphology characteristics. While the morphology of an important proportion of SnO₂ nanocrystals evolve into nanowires after the surface ligand exchanged, as shown in Fig. 2(d, e). It may be ascribed to the self-assembly during the procedure of ligand exchange. Fig. 2(c) and Fig. 2(f) display the SAED (selected area electron diffraction) patterns of OA-capped SnO₂ and BF₄⁻-capped SnO₂. Both SAED patterns exhibit clearly visible diffraction rings, suggesting highly crystallinity. The electron diffraction rings can be well indexed to the (110), (101) and (211) planes of rutile SnO₂, which is in good agreement with the results deduced from XRD tests [36,37]. The HRTEM images and SAED patterns in Fig. 2 reveal that introducing long hydrocarbon molecule (OA) into reaction precursor is conductive to the formation of SnO₂ nanocrystals with uniform size and controlled morphologies, yet the ligand exchange process significantly changes the situation. Especially, it needs to be pointed out that the change of morphology did not affect the dispersion quality of SnO₂ colloid.

3.3. The effects of ligands coated on SnO₂ ETLs on the crystallization process of perovskite light-absorption layer

Fig. S1 shows the contact angle measurements for the perovskite precursor solutions on different SnO₂ ETLs. It can be observed that the sample of perovskite precursor solution on BF₄⁻-capped SnO₂ ETL exhibits a much smaller contact angle, indicating that changing the ligands from OA to BF₄⁻ can significantly improve the wettability of perovskite precursor. As reported, the wettability of perovskite precursor on ETL plays an essential role in the crystallization process of perovskite light-absorption layer [38,39]. Consequently, the XRD patterns and FESEM images of perovskite layers on different SnO₂ substrates were carried out.

Fig. S2 shows the XRD patterns of perovskite layers on different SnO₂ ETLs. Both of the samples show the same diffraction peak positions, indicating that the ligand exchange process of SnO₂ has no significant effect on the formation of perovskite crystal phase. The FESEM images of perovskite layers on different SnO₂ ETLs are shown in Fig. S3. As depicted, the particle size of perovskite deposited on BF₄⁻-capped SnO₂ ETL is much more uniform than that deposited on OA-capped SnO₂ ETL. The results in Figs. S1–S3 reveals that ligand exchange process improve the wettability of perovskite precursor solution on SnO₂ ETL, promoting the formation of perovskite nanoparticles with more uniform size.

3.4. Photovoltaic performance

Fig. 3(a) presents the photovoltaic performance of the champion *f*-PSCs based on different SnO₂ ETLs measured under reverse scan. The extracted photovoltaic parameters are provided in Table 1. As displayed, the *f*-PSC based on OA-capped SnO₂ ETL exhibits a maximum PCE value of 13.71%, with short-circuit current density (J_{SC}) value of 20.12 mA cm⁻², open-circuit voltage (V_{OC}) value of 1.063 V and fill factor (FF) value of 0.641. After ligand exchange, the champion device achieves a markedly improved PCE of 17.96% with J_{SC} value of 21.43 mA cm⁻², V_{OC} value of 1.116 V and FF value of 0.751. The results in J-V curves depict that removing insulating OA ligand can significantly improve the photovoltaic performance of *f*-PSC devices, which is attributed to the reduction of electronic barriers resulting from OA ligand after ligands interchange reaction. Fig. 3(b) presents the EQE spectra. It can be seen that both devices show wide

photo-response. By comparison, obvious increase can be observed when using the BF₄⁻-capped SnO₂ as ETL. The integrated J_{SC} values derived from EQE spectra for the *f*-PSCs with OA-capped SnO₂ ETL and BF₄⁻-capped SnO₂ ETL are 18.17 and 19.14 mA cm⁻², respectively, which is very close to the values measured by J-V curves. Fig. 3(c) shows the stabilized power output of the two kinds of *f*-PSCs at each maximum power point voltage. The photocurrent density of *f*-PSC with OA-capped SnO₂ ETL is constant at 15.73 mA cm⁻² over a period of 400 s, yielding a stabilized PCE of 11.80%. However, the BF₄⁻-capped SnO₂ based *f*-PSC acquires an improved stabilized PCE of 16.31% with photocurrent density of 18.53 mA cm⁻², indicating that the device can work effectively under actual working conditions.

3.5. Photoelectrochemical properties

To clarify the carrier extraction and transportation behavior at the interface of perovskite light absorption layer and SnO₂ ETL, SSPL and TRPL measurements were carried out by using the sample structure of PET/OA(or BF₄⁻)-capped SnO₂/perovskite. The SSPL spectra were conducted with 485 nm photo-excitation and the TRPL spectra were measured with an excitation wavelength of 485 nm. Fig. 4(a) is the SSPL spectra. Generally, the quenching intensity is related to the extraction of photo-generated electrons across the interface of perovskite layer and ETL [40,41]. As represented in Fig. 4(a), the fluorescence quenching intensity of BF₄⁻-capped SnO₂ sample is stronger than that of OA-capped SnO₂, indicating that BF₄⁻-capped SnO₂ ETL has more effective charge carrier extraction efficiency. This means that the electronic barriers resulted from OA ligands compromise charge transport, which can be significantly improved after replacing the long OA ligands with BF₄⁻. Fig. 4(b) is the TRPL spectra. The PL decay curves can be fitted with bi-exponential decay equation and the relevant data are shown in Table 2. Generally, the slow τ₁ is ascribed to the radiative recombination, the fast τ₂ is caused by the quenching of charge carriers at the interface between carrier transport layer and perovskite layer [42]. So τ₂ is the focus of our attention. According to Table 2, the τ₂ value for the sample of perovskite layer on BF₄⁻-capped SnO₂ ETL decreases to 9.93 ns compared to 29.58 ns for the sample of perovskite layer on OA-capped SnO₂ ETL, clearly manifesting that less electronic barriers exist at the interface between perovskite and BF₄⁻-capped SnO₂ ETL and the photo-generated electrons can be more effectively extracted from perovskite layer to BF₄⁻-capped SnO₂ ETL. These results demonstrate that reducing insulating OA ligands on SnO₂ surface helps to reduce barriers and can effectively boost the carriers transfer at the interface of perovskite and SnO₂ ETL, which further improves the photovoltaic performance of *f*-PSC.

Fig. 4(c, d) depicts the TPC and TPV response curves of *f*-PSCs with different SnO₂ ETLs. From which we can obtain the charge transport time (τ_t) and charge recombination lifetime (τ_r). The *f*-PSC based on BF₄⁻-capped SnO₂ ETL gets reduced photocurrent decay time (τ_t = 0.84 μs) by contrast with that of the device assembled with OA-capped SnO₂ ETL (τ_t = 1.17 μs), signifying faster charge carrier transport. Furthermore, the BF₄⁻-capped SnO₂ based *f*-PSC shows a higher photovoltage decay time of 853.85 μs, implying slower surface charge recombination. The TPC and TPV results manifest that an improved electron extraction efficiency occurs in the *f*-PSC based on BF₄⁻-capped SnO₂ ETL. The results are in accordance with the conclusion from SSPL and TRPL.

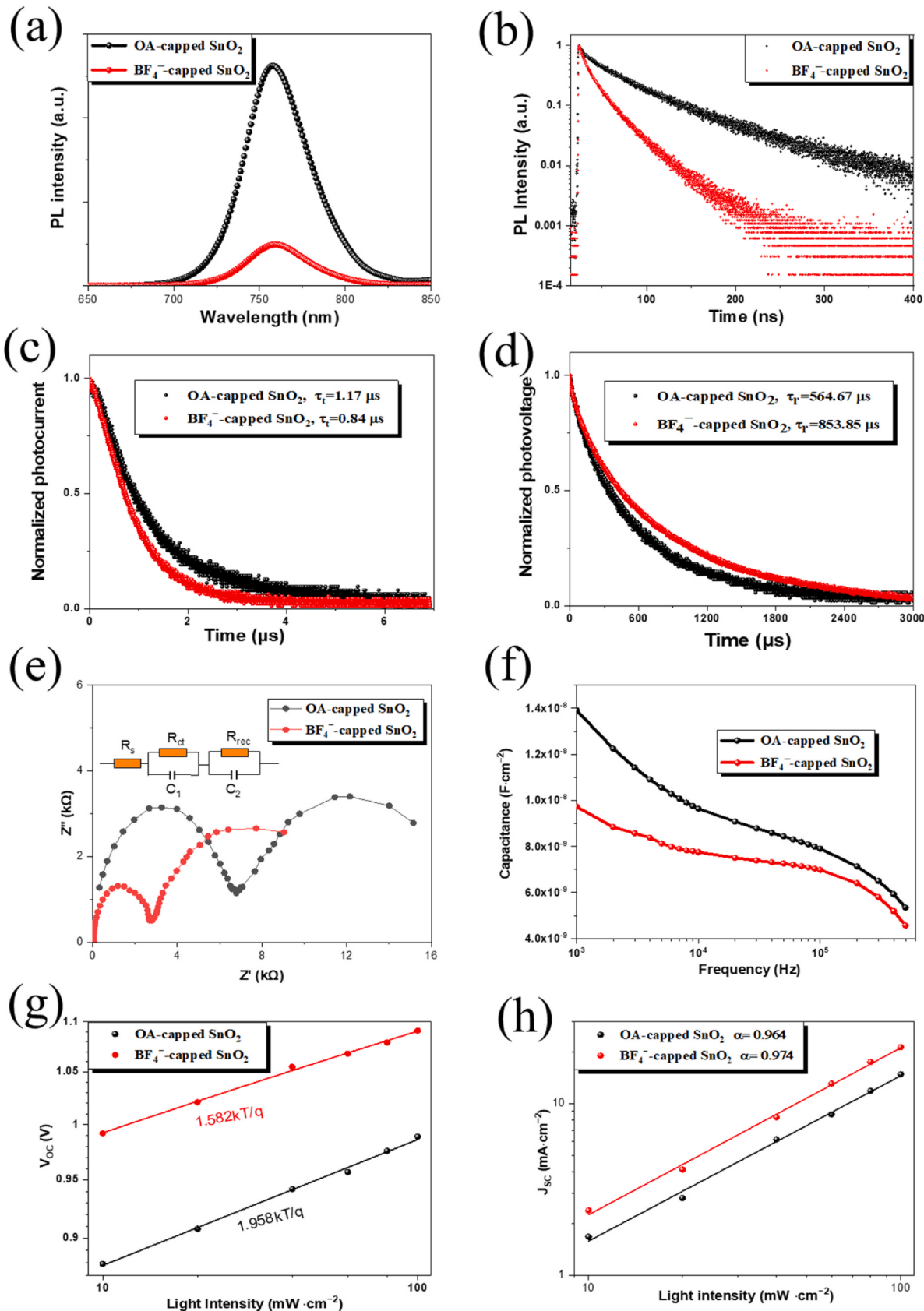


Fig. 4. (a) SSPL spectra for PET/OA (or BF_4^-)-capped SnO_2 /perovskite, (b) TRPL spectra for PET/OA (or BF_4^-)-capped SnO_2 /perovskite, (c) normalized TPC curves of the f-PSCs with different SnO_2 ETLs, (d) normalized TPV curves of the f-PSCs with different SnO_2 ETLs, (e) Nyquist plots of f-PSCs based on different SnO_2 ETLs, the inset is the equivalent circuit used for fitting, (f) C-F curves of the f-PSCs based on different SnO_2 ETLs, (g) dependence of V_{OC} on light intensity for the f-PSCs with different SnO_2 ETLs, (h) dependence of J_{SC} on light intensity for the f-PSCs with different SnO_2 ETLs.

Table 2

Parameters obtained from TRPL spectra.

ETLs	τ_1 (ns)	A ₁ (%)	τ_2 (ns)	A ₂ (%)	τ_{ave} (ns)
OA-capped SnO ₂	83.48	72.13	29.58	27.87	68.44
BF ₄ ⁻ -capped SnO ₂	32.25	62.11	9.93	37.89	23.79

EIS was conducted to study the charge transport and transfer behavior in f-PSCs. The relevant Nyquist plots and the corresponding equivalent circuit are displayed in Fig. 4(e). Both plots show two semicircles. Generally, the series resistance (R_s) can be obtained from the intercept on the real axis in high frequency region. The first semicircle at high frequency region is mainly in connection with the charge transfer resistance (R_{tr}) and the second semicircle at low frequency region primarily corresponds to the recombination resistance (R_{rec}) [43]. As displayed, the f-PSC based on BF₄⁻-capped SnO₂ ETL, on one hand, exhibits significantly reduced R_{tr} value, indicating that the device has dramatically improved charge transfer capability. On the other hand, it remains high R_{rec} value, which means that it has low recombination loss. The ameliorative charge transfer property and the ability to effectively inhibit carrier recombination contribute to the improvement of photovoltaic performance of f-PSC. The improved charge transfer at the interface of perovskite layer and SnO₂ ETL was further verified by C-F curves. According to the previous reports, the capacitance is associated with the ionic and charge accumulation across the interface [43,44]. As shown in Fig. 4(f), the trend of the curves suggests that the value of the low-frequency capacitance for the f-PSC with BF₄⁻-capped SnO₂ ETL is smaller than that of the f-PSC with OA-capped SnO₂ ETL, which means that the ionic and charge accumulation get decreased after ligand exchange procedure, thus leading to the enhanced photovoltaic performance.

To gain more insight into the charge carrier recombination kinetics, the dependence of V_{OC} and J_{SC} on light intensity was tested respectively. Fig. 4(g) shows the relationship of V_{OC} and logarithmic light intensity. In the plot, the slope is an important parameter as it reflects the recombination situation in PSCs. For an ideal PSC system (only have radiative recombination and the leakage current is negligible), the slope is equal to kT/q (k is the Boltzmann constant, T is the absolute temperature, q is the electronic charge). If the slope is larger, trap-assisted carrier recombination happens [45,46]. In Fig. 4(g), it can be observed that both V_{OC} increase monotonically with light intensity. After linear fitting, the slope for BF₄⁻-capped SnO₂ based f-PSC is calculated as 1.582 which is much smaller than that of the OA-capped SnO₂ based device (1.958), demonstrating a significantly suppression of trap-assisted charge recombination. Fig. 4(h) presents the linear relationship of logarithmic J_{SC} and logarithmic light intensity. For space-charge unlimited PSC device, the slope close to 1, otherwise it approaches to 0.75 [47,48]. As shown in Fig. 4(h), the fitted slopes for OA-capped SnO₂ based f-PSC and BF₄⁻-capped SnO₂ based f-PSC are 0.964 and 0.974, respectively, manifesting that the space-charge buildup situation in BF₄⁻-capped SnO₂ based f-PSC gets significantly improved. That is to say, compared to the f-PSC based on OA-capped SnO₂ ETL, the charge carrier transport in BF₄⁻-capped SnO₂ based f-PSC is more balanced as more excited electrons are delivered before recombination.

4. Conclusions

In this work, we elucidate a new approach to fabricate SnO₂ ETL for f-PSC. At first, the re-dispersible SnO₂ nanocrystals were fabricated by solvothermal method with the assistance of OA molecules. Afterwards, the OA molecules that impair the photovoltaic performance of f-PSC were stripped by ligand exchange process. The removal of OA ligands enhanced the interparticle interaction in SnO₂ ETL, decreasing the

electron transfer resistance, resulting in remarkably enhanced photovoltaic performance. The resulted f-PSC device achieves an efficiency of 17.96%. This work opens up a new avenue to fabricate SnO₂-based flexible perovskite photovoltaic devices.

CRediT authorship contribution statement

Jia Dong: Methodology, Validation, Formal analysis, Writing - original draft. **Jinbiao Jia:** Conceptualization, Writing - review & editing, Formal analysis. **Xu Feng:** Investigation, Methodology. **Beibei Shi:** Investigation, Validation. **Yangqing Wu:** Formal analysis. **Yongzheng Zhang:** Formal analysis. **Jihuai Wu:** Project administration, Funding acquisition, Supervision. **Bingqiang Cao:** Project administration, Funding acquisition, Supervision.

Declaration of Competing Interest

The authors declare that they have no known competing financial interests or personal relationships that could have appeared to influence the work reported in this paper.

Acknowledgment

The work was supported by the Natural Science Foundation of Shandong Province (ZR2019BF025), National Natural Science Foundation of China (No. 51872161) and Open Fund of Fujian Key Laboratory of Photoelectric Functional Materials (Huqiao University) (FJPFM-201901).

Appendix A. Supplementary material

Supplementary data associated with this article can be found in the online version at doi:10.1016/j.jallcom.2021.160827.

References

- [1] A. Kojima, K. Teshima, Y. Shirai, T. Miyasaka, Organometal halide perovskites as visible-light sensitizers for photovoltaic cells, *J. Am. Chem. Soc.* 131 (2009) 6050–6051.
- [2] H.-S. Kim, C.-R. Lee, J.-H. Im, K.-B. Lee, T. Moehl, A. Marchioro, S.-J. Moon, R. Humphry-Baker, J.-H. Yum, J.E. Moser, M. Grätzel, N.-G. Park, Lead iodide perovskite sensitized all-solid-state submicron thin film mesoscopic solar cell with efficiency exceeding 9%, *Sci. Rep.* 2 (2012) 591.
- [3] M.M. Lee, J. Teuscher, T. Miyasaka, T.N. Murakami, H.J. Snaith, Efficient hybrid solar cells based on meso-superstructured organometal halide perovskites, *Science* 338 (2012) 643–647.
- [4] J. Burschka, N. Pellet, S.J. Moon, R. Humphry-Baker, P. Gao, M.K. Nazeeruddin, M. Grätzel, Sequential deposition as a route to high-performance perovskite-sensitized solar cells, *Nature* 499 (2013) 316–319.
- [5] Z. Chen, B. Turedi, A.Y. Alsalloum, C. Yang, X. Zheng, I. Gereige, A. AlSaggaf, O.F. Mohammed, O.M. Bakr, Single-crystal MAPbI₃ perovskite solar cells exceeding 21% power conversion efficiency, *ACS Energy Lett.* 4 (2019) 1258–1259.
- [6] K. Huang, Y. Peng, Y. Gao, J. Shi, H. Li, X. Mo, H. Huang, Y. Gao, L. Ding, J. Yang, High-performance flexible perovskite solar cells via precise control of electron transport layer, *Adv. Energy Mater.* 9 (2019) 1901419.
- [7] K. Yoshikawa, H. Kawasaki, W. Yoshida, T. Irie, K. Konishi, K. Nakano, T. Uto, D. Adachi, M. Kanematsu, H. Uzu, K. Yamamoto, Silicon heterojunction solar cell with interdigitated back contacts for a photoconversion efficiency over 26%, *Nat. Energy* 2 (2017) 17032.
- [8] Best Research-Cell Efficiency Chart, 2021. <https://www.nrel.gov/pv/cell-efficiency.html>.
- [9] C. Liu, J. Sun, X.F. Jiang, L. Huang, Z. Ge, A universal tactic of using Lewis-base polymer-CNTs composites as additives for high performance cm²-sized and flexible perovskite solar cells, *Sci. China Chem.* 64 (2020).
- [10] Q. Sun, H. Li, X. Gong, H. Ban, Y. Shen, M. Wang, Interconnected SnO₂ nanocrystals electron transport layer for highly efficient flexible perovskite solar cells, *Sol. RRL* 4 (2020) 1900229.
- [11] J. Jia, J. Dong, J. Lin, Z. Lan, L. Fan, J. Wu, Improved photovoltaic performance of perovskite solar cells by utilizing down-conversion NaYF₄:Eu³⁺ nanophosphors, *J. Mater. Chem. C* 7 (2019) 937–942.
- [12] X. Li, C. Li, Y. Wu, J. Cao, Y. Tang, A reaction-and-assembly approach using monoamine zinc porphyrin for highly stable large-area perovskite solar cells, *Sci. China Chem.* 63 (2020) 777–784.
- [13] L. Yang, Y. Xiao, G. Han, Y. Chang, Y. Zhang, W. Hou, J.-Y. Lin, H. Li, The ZATT-TOP2A-PICH axis drives extensive replication fork reversal to promote genome stability, *Mol. Cell* 81 (2021) 198–211.

- [14] Y. Cai, J. Cui, M. Chen, M. Zhang, Y. Han, F. Qian, H. Zhao, S. Yang, Z. Yang, H. Bian, T. Wang, K. Guo, M. Cai, S. Dai, Z. Liu, S. Liu, Multifunctional enhancement for highly stable and efficient perovskite solar cells, *Adv. Funct. Mater.* 31 (2021) 2005776.
- [15] K. Huang, Y. Peng, Y. Gao, J. Shi, H. Li, X. Mo, H. Huang, Y. Gao, L. Ding, J. Yang, High-performance flexible perovskite solar cells via precise control of electron transport layer, *Adv. Energy Mater.* 9 (2019) 1901419.
- [16] M. Zhong, Y. Liang, J. Zhang, Z. Wei, Q. Li, D. Xu, Highly efficient flexible MAPbI₃ solar cells with a fullerene derivative-modified SnO₂ layer as the electron transport layer, *J. Mater. Chem. A* 7 (2019) 6659–6664.
- [17] M.R. Kim, H.W. Choi, C.W. Bark, Low-temperature thermally evaporated SnO₂ based electron transporting layer for perovskite solar cells with annealing process, *J. Nanosci. Nanotechnol.* 20 (2020) 5491–5497.
- [18] Z. Song, W. Bi, X. Zhuang, Y. Wu, B. Zhang, X. Chen, C. Chen, Q. Dai, H. Song, Low-temperature electron beam deposition of Zn-SnO_x for stable and flexible perovskite solar cells, *Sol. RRL* 4 (2020) 1900266.
- [19] C. Wang, D. Zhao, C.R. Grice, W. Liao, Y. Yu, A. Cimaroli, N. Shrestha, P.J. Roland, J. Chen, Z. Yu, P. Liu, N. Cheng, R.J. Ellingson, X. Zhao, Y. Yan, Low-temperature plasma-enhanced atomic layer deposition of tin oxide electron selective layers for highly efficient planar perovskite solar cells, *J. Mater. Chem. A* 4 (2016) 12080–12087.
- [20] Y. Kuang, V. Zardetto, R. van Gils, S. Karwal, D. Koushik, M.A. Verheijen, L.E. Black, C. Weijtens, S. Veenstra, R. Andriessen, W.M.M. Kessels, M. Creatore, Low-temperature plasma-assisted atomic-layer-deposited SnO₂ as an electron transport layer in planar perovskite solar cells, *ACS Appl. Mater. Interfaces* 10 (2018) 30367–30378.
- [21] W. Ke, D. Zhao, A.J. Cimaroli, C.R. Grice, P. Qin, Q. Liu, L. Xiong, Y. Yan, G. Fang, Effects of annealing temperature of tin oxide electron selective layers on the performance of perovskite solar cells, *J. Mater. Chem. A* 3 (2015) 24163–24168.
- [22] C. Liu, L. Zhang, X. Zhou, J. Gao, W. Chen, X. Wang, B. Xu, Hydrothermally treated SnO₂ as the electron transport layer in high-efficiency flexible perovskite solar cells with a certificated efficiency of 17.3%, *Adv. Funct. Mater.* 29 (2019) 1807604.
- [23] Q. Dong, J. Li, Y. Shi, M. Chen, L.K. Ono, K. Zhou, C. Zhang, Y. Qi, Y. Zhou, N.P. Padture, L. Wang, Improved SnO₂ electron transport layers solution-deposited at near room temperature for rigid or flexible perovskite solar cells with high efficiencies, *Adv. Energy Mater.* 9 (2019) 1900834.
- [24] X. Zhang, T. Wu, X. Xu, L. Zhang, J. Tang, X. He, J. Wu, Z. Lan, Ligand-exchange TiO₂ nanocrystals induced formation of high-quality electron transporting layers at low temperature for efficient planar perovskite solar cells, *Sol. Energy Mater. Sol. Cells* 178 (2018) 65–73.
- [25] J. Jia, J. Dong, J. Wu, H. Wei, B. Cao, Combustion procedure deposited SnO₂ electron transport layers for high efficient perovskite solar cells, *J. Alloy. Compd.* 844 (2020) 156032.
- [26] J. Jia, J. Dong, B. Shi, J. Wu, Y. Wu, B. Cao, Postpassivation of Cs_{0.05}(FAO.83MAO.17)0.95Pb(I0.83Br0.17)3 perovskite films with tris(pentafluorophenyl)borane, *ACS Appl. Mater. Interfaces* 13 (2021) 2472–2482.
- [27] Z. Lan, X. Xu, X. Zhang, J. Tang, L. Zhang, X. He, J. Wu, Low-temperature solution-processed efficient electron-transporting layers based on BF₄-capped TiO₂ nanorods for high-performance planar perovskite solar cells, *J. Mater. Chem. C* 6 (2018) 334–341.
- [28] J. Xu, A. Gulzar, Y. Liu, H. Bi, S. Gai, B. Liu, D. Yang, F. He, P. Yang, Integration of IR-808 sensitized upconversion nanostructure and MoS₂ nanosheet for 808 nm NIR light triggered phototherapy and bioimaging, *Small* 13 (2017) 1701841.
- [29] F.X. Hu, K.G. Neoh, E.T. Kang, Synthesis and in vitro anti-cancer evaluation of tamoxifen-loaded magnetite/PLLA composite nanoparticles, *Biomaterials* 27 (2006) 5725–5733.
- [30] D. Wilson, M.A. Langell, XPS analysis of oleylamine/oleic acid capped Fe3O4 nanoparticles as a function of temperature, *Appl. Surf. Sci.* 303 (2014) 6–13.
- [31] X. Meng, M. Zhou, X. Li, J. Yao, F. Liu, H. He, P. Xiao, Y. Zhang, Synthesis of SnO₂ nanoflowers and electrochemical properties of Ni/SnO₂ nanoflowers in supercapacitor, *Electrochim. Acta* 109 (2013) 20–26.
- [32] B. Zhang, Q.B. Zheng, Z.D. Huang, S.W. Oh, J.K. Kim, SnO₂-graphene-carbon nanotube mixture for anode material with improved rate capacities, *Carbon* 49 (2011) 4524–4534.
- [33] P. Hanyš, P. Janeček, V. Matolín, G. Korotcenkov, V. Nehasil, XPS and TPD study of Rh/SnO₂ system – reversible process of substrate oxidation and reduction, *Surf. Sci. Sci.* 600 (2006) 4233–4238.
- [34] I.M. Costa, Y.N. Colmenares, P.S. Pizani, E.R. Leite, A.J. Chiquito, Sb doping of VLS synthesized SnO₂ nanowires probed by Raman and XPS spectroscopy, *Chem. Phys. Lett.* 695 (2018) 125–130.
- [35] P.S. Shewale, K. Ung Sim, Y.-b Kim, J.H. Kim, A.V. Moholkar, M.D. Uplane, Structural and photoluminescence characterization of SnO₂: F thin films deposited by advanced spray pyrolysis technique at low substrate temperature, *J. Lumin.* 139 (2013) 113–118.
- [36] X. Xu, Z. Xu, J. Tang, X. Zhang, L. Zhang, J. Wu, Z. Lan, High-performance planar perovskite solar cells based on low-temperature solution-processed well-crystalline SnO₂ nanorods electron-transporting layers, *Chem. Eng. J.* 351 (2018) 391–398.
- [37] E. Wang, P. Chen, X. Yin, Y. Wu, W. Que, Tailoring electronic properties of SnO₂ quantum dots via aluminum addition for high-efficiency perovskite solar cells, *Sol. RRL* 3 (2019) 1900041.
- [38] Y. Ming, M. Xu, S. Liu, D. Li, Q. Wang, X. Hou, Y. Hu, Y. Rong, H. Han, Ethanol stabilized precursors for highly reproducible printable mesoscopic perovskite solar cells, *J. Power Sources* 424 (2019) 261–267.
- [39] W. Tang, Y. Chen, J. Yang, R. Yuan, Y. Lv, Q. Ma, Y. Wu, P. Zhang, W.-H. Zhang, Acetone-assisted precursor engineering enables low-temperature fabrication of CsPbI₂Br perovskite for efficient solar cells, *J. Power Sources* 482 (2021) 228965.
- [40] Z. Wang, D.P. McMeekin, N. Sakai, S. van Reenen, K. Wojciechowski, J.B. Patel, M.B. Johnston, H.J. Snaith, Efficient and air-stable mixed-cation lead mixed-halide perovskite solar cells with n-doped organic electron extraction layers, *Adv. Mater.* 29 (2017) 1604186.
- [41] B. Du, Q. Wei, Y. Cai, T. Liu, B. Wu, Y. Li, Y. Chen, Y. Xia, G. Xing, W. Huang, Crystal face dependent charge carrier extraction in TiO₂/perovskite heterojunctions, *Nano Energy* 67 (2020) 104227.
- [42] D. Yang, R. Yang, K. Wang, C. Wu, X. Zhu, J. Feng, X. Ren, G. Fang, S. Priya, S. Liu, High efficiency planar-type perovskite solar cells with negligible hysteresis using EDTA-complexed SnO₂, *Nat. Commun.* 9 (2018) 3239.
- [43] Q. Guo, J. Wu, Y. Yang, X. Liu, W. Sun, Y. Wei, Z. Lan, J. Lin, M. Huang, H. Chen, Y. Huang, Low-temperature processed rare-earth doped brookite TiO₂ scaffold for UV stable, hysteresis-free and high-performance perovskite solar cells, *Nano Energy* 77 (2020) 105183.
- [44] F. Wang, M. Yang, Y. Zhang, J. Du, D. Han, L. Yang, L. Fan, Y. Sui, Y. Sun, X. Meng, J. Yang, Constructing m-TiO₂/a-WO_x hybrid electron transport layer to boost interfacial charge transfer for efficient perovskite solar cells, *Chem. Eng. J.* 402 (2020) 126303.
- [45] T. Bu, J. Li, F. Zheng, W. Chen, X. Wen, Z. Ku, Y. Peng, J. Zhong, Y. Cheng, F. Huang, Universal passivation strategy to slot-die printed SnO₂ for hysteresis-free efficient flexible perovskite solar module, *Nat. Commun.* 9 (2018) 4609.
- [46] Z. Yang, W. Chen, A. Mei, Q. Li, Y. Liu, Flexible MAPbI₃ perovskite solar cells with the high efficiency of 16.11% by low-temperature synthesis of compact anatase TiO₂ film, *J. Alloy. Compd.* (2020) 155488.
- [47] X. Liu, P. Li, Y. Zhang, X. Hu, Y. Duan, F. Li, D. Li, G. Shao, Y. Song, High-efficiency perovskite solar cells based on self-assembly n-doped fullerene derivative with excellent thermal stability, *J. Power Sources* 413 (2019) 459–466.
- [48] J. Zhang, B. Hu, Revealing photoinduced bulk polarization and spin-orbit coupling effects in high-efficiency 2D/3D Pb-Sn alloyed perovskite solar cells, *Nano Energy* 76 (2020) 104999.